JACS
JOURNAL OF THE AMERICAN CHEMICAL SOCIETY
Communication
pubs.acs.org/JACS

Transformative Evolution of Organolead Triiodide Perovskite Thin Films from Strong Room-Temperature Solid–Gas Interaction between $HPbI_3$-CH_3NH_2 Precursor Pair

Shuping Pang,[†,#] Yuanyuan Zhou,[‡,#] Zaiwei Wang,[†,#] Mengjin Yang,[§] Amanda R. Krause,[‡] Zhongmin Zhou,[†] Kai Zhu,[*,§] Nitin P. Padture,[*,‡] and Guanglei Cui[*,†]

[†]Qingdao Institute of Bioenergy and Bioprocess Technology, Chinese Academy of Sciences, Qingdao 266101, P.R. China
[‡]School of Engineering, Brown University, Providence, Rhode Island 02912, United States
[§]Chemistry and Nanoscience Center, National Renewable Energy Laboratory, Golden, Colorado 80401, United States

Supporting Information

ABSTRACT: We demonstrate the feasibility of a nonsalt-based precursor pair—inorganic $HPbI_3$ solid and organic CH_3NH_2 gas—for the deposition of uniform $CH_3NH_3PbI_3$ perovskite thin films. The strong room-temperature solid–gas interaction between $HPbI_3$ and CH_3NH_2 induces transformative evolution of ultrasmooth, full-coverage perovskite thin films at a rapid rate (in seconds) from nominally processed rough, partial-coverage $HPbI_3$ thin films. The chemical origin of this behavior is elucidated via *in situ* experiments. Perovskite solar cells, fabricated using $MAPbI_3$ thin films thus deposited, deliver power conversion efficiencies up to 18.2%, attesting to the high quality of the perovskite thin films deposited using this transformative process.

Since the use of methylammonium lead triiodide ($CH_3NH_3PbI_3$ or $MAPbI_3$) perovskite as the light absorber material in solar cells by Kojima et al. in 2009,[1] the power conversion efficiency (PCE) of perovskite solar cells (PSCs) has shot up rapidly within a short period of time.[2] The rapid advances in PSCs are enabled by enhanced control over the formation of uniform $MAPbI_3$ absorber films via myriad processing methods.[3,4] In particular, the sequential deposition method, where the formation of the $MAPbI_3$ occurs by reaction between the organic precursor with the predeposited inorganic precursor counterpart, has gained wide popularity.[4] An unprecedented amount of effort has been devoted to developing this method, and its variations, for improving the quality of resultant $MAPbI_3$ films, but it has yielded mixed results.[4−6] All this effort invariably involves precursor pairs consisting of an inorganic lead salt and an organic methylammonium salt, with the PbI_2-MAI pair being the most typical example.[4−6] The reaction, $PbI_2 + MAI \rightarrow MAPbI_3$, involves the formation of new Pb−I bonds toward the construction of the 3D perovskite structure, and it is regarded as a neutralization reaction of the electrophile (acid) PbI_2 with the nucleophile (base) MAI,[7] but the acidity/basicity of these two salts is low. Thus, the mutual interaction between salts-based precursors is expected to be relatively weak. Also, the insertion kinetics of MAI species into 2D layered PbI_6^{4-} octahedral arrays of PbI_2, especially in its bulk form, is sluggish considering the long diffusion pathways and the reconstructive nature of the 2D → 3D structural transformation. Furthermore, the use of certain solvents (e.g., isopropanol) usually associated with this process has a detrimental effect on the morphology of the final perovskite films.[4,5]

These considerations provide the motivation for discovering new precursor pairs that (i) exhibit strong mutual interaction, (ii) enhance perovskite-crystallization kinetics, and (iii) avoid the use of liquid solvents. In this context, inspection of the stoichiometry of $MAPbI_3$ suggests a new possible precursor pair consisting of hydrogen lead triiodide ($HPbI_3$) as the inorganic component and methylamine gas (CH_3NH_2) as the organic component. The synthesis of $HPbI_3$ was first reported by Zhao et al.,[8] but in this study we have used an antisolvent-crystallization method[9] (described in the Supporting Information (SI)) based on stoichiometric PbI_2/HI precursors for obtaining excellent quality $HPbI_3$ crystals. Pawley fitting of the X-ray diffraction (XRD) pattern of these $HPbI_3$ crystals (powder) in Figure 1A shows an orthorhombic (space group $P6_3mc$) structure with lattice parameters $a = b = 8.765(1)$ Å, $c = 8.177(2)$ Å. This is further supported by the high-resolution transmission electron microscopy (HR-TEM) image of $HPbI_3$, solution deposited onto a TEM grid directly, shown in Figure 1A (inset). The lattice fringes with interplanar distance of 0.62 nm can be assigned to (110) planes of the orthorhombic $HPbI_3$ crystal. (Note: The H atom that is intercalated into the orthorhombic crystal is not considered for the symmetry here; more detailed characterization is underway for further elucidation of the complete crystal structure of $HPbI_3$.) The other precursor in the new pair, CH_3NH_2, has a boiling point of −6.8 °C and is a gas at room temperature. Thus, to demonstrate the feasibility of $MAPbI_3$ perovskite formation using this new precursor pair, the solid $HPbI_3$ powder is simply exposed to the CH_3NH_2 gas and is then removed from the gas. The light-yellow $HPbI_3$ powder is converted into a black phase when this process is complete. The Pawley fit of the XRD pattern (Figure 1B) of the resultant black phase confirms tetragonal $MAPbI_3$ perovskite (space group $I4/mcm$; lattice parameters $a = b = 8.873(1)$ Å, $c = 12.662(1)$ Å). The HR-TEM images in Figure 1B (inset) shows lattice fringes with interplanar distance of 0.44 nm, corresponding to (112) or (020) planes in $MAPbI_3$ perovskite. These results

Received: November 11, 2015
Published: January 5, 2016

DOI: 10.1021/jacs.5b11824
J. Am. Chem. Soc. 2016, 138, 750−753

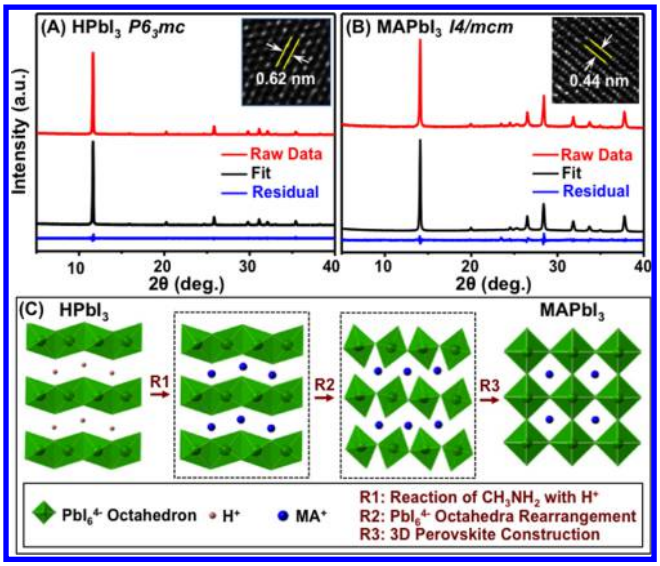

Figure 1. XRD pattern and the Pawley fit, and HR-TEM image (inset) of: (A) $HPbI_3$ powder and (B) $MAPbI_3$ powder converted from the $HPbI_3$ powder after CH_3NH_2-gas treatment. (C) Schematic illustration of crystallographic conversion from $HPbI_3$ to $MAPbI_3$ upon reaction with CH_3NH_2.

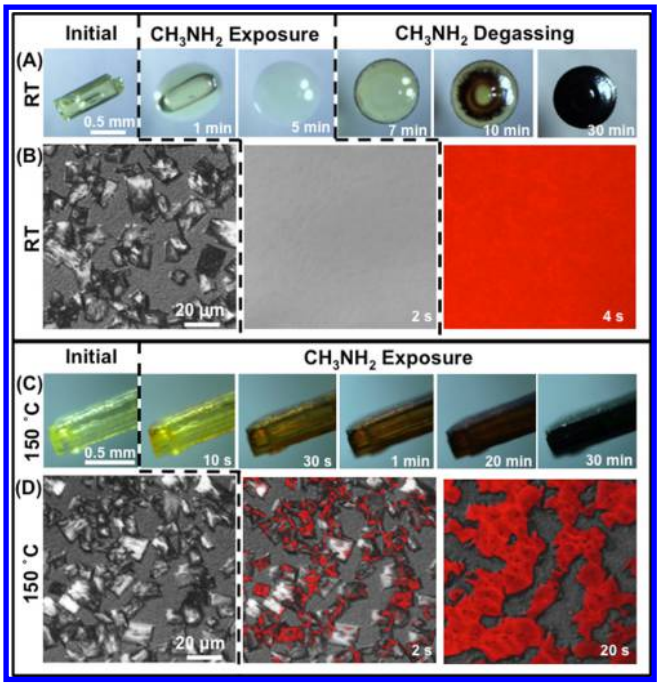

Figure 2. *In situ* optical microscopic observation of the morphological evolution of a $HPbI_3$ crystal during interaction with CH_3NH_2 gas: (A) at room temperature (RT) and (C) at 150 °C. *In situ* PL maps (superimposed on optical microscopic images) of $HPbI_3$ thin film during interaction with CH_3NH_2 gas: (B) at RT and (D) at 150 °C. The elapsed time is indicated.

clearly show the conversion of $HPbI_3$ crystalline phase to $MAPbI_3$ perovskite with CH_3NH_2-gas treatment.

The possible crystallographic conversion mechanism from $HPbI_3$ to $MAPbI_3$ is shown schematically in Figure 1C. The pseudo-3D crystal structure of $HPbI_3$ consists of arrays of 1D face-shared PbI_6^{4-} octahedra with intercalated protons (H^+) for charge balance. Upon exposure to CH_3NH_2 gas, the CH_3NH_2 molecules readily react with H^+ via the reaction, $CH_3NH_2 + H^+ \rightarrow CH_3NH_3^+$, with enhanced affinity toward the 1D face-shared PbI_6^{4-} octahedra chains. Once the adjacent 1D PbI_6^{4-} octahedra chain come close enough to each other, the Pb^{2+} cation from each array shares an I^- anion to form a linear Pb−I−Pb bond. As a result, the H^+-intercalated 1D structure with face-shared PbI_6^{4-} octahedra transitions into 3D perovskite structure with corner-shared PbI_6^{4-} octahedra. It is obvious that H^+ plays an important role in the stoichiometric formation of $MAPbI_3$ perovskite, which is further supported by the fact that stable perovskite phase could not be formed using a KI−PbI_2 system instead of $HPbI_3$ (see Figure S1).

The new $HPbI_3$-CH_3NH_2 precursor pair for the formation of $MAPbI_3$ perovskite has the following unique characteristics, as compared with the conventional PbI_2-MAI precursor pair. First, the perovskite formation is driven by the strong acid−base interaction between H^+ with the CH_3NH_2. Second, the gaseous nature of CH_3NH_2 allows highest contact area with the $HPbI_3$ solid precursor and facilitates the reaction, precluding the need for solvents[4] or thermally induced ionization[6] that are typically needed for making the MAI phase more reactive in salt-based precursor pairs. Finally, in the $HPbI_3$ structure, Pb−I bonds are fully formed, whereas the intercalation reaction of PbI_2 with MAI entails the formation of new Pb−I bonds in the conventional precursor pair case. Thus, a near-topotactic conversion[10] of the $HPbI_3$ crystal structure to $MAPbI_3$ perovskite occurs, as illustrated in Figure 1C.

In order to gain insight into the details of the $HPbI_3$-to-$MAPbI_3$ phase conversion process and the associated morphological evolution, a combination of *in situ* optical and photoluminescence (PL) microscopies is used. Figure 2A shows the evolution of a rod-like $HPbI_3$ crystal (typical morphology for solution-grown $HPbI_3$) into a $MAPbI_3$ particle using optical microscopy. Upon exposure to CH_3NH_2 gas at room temperature for 5 min, the $HPbI_3$ crystal gradually turns into a liquid phase. Upon removal of the CH_3NH_2 gas at room temperature, the liquid drop gradually crystallizes into $MAPbI_3$ perovskite (30 min), as confirmed by XRD in Figure 1B. Since $HPbI_3$, the intermediate liquid phase, and $MAPbI_3$ perovskite have obviously distinct PL responses, *in situ* PL microscopy is an ideal tool for following the evolution of these phases during the reaction in thin films. Here, $HPbI_3$ dissolved in DMF solvent is spin-coated (60 wt %, 6000 rpm, 20 s) onto a glass substrate and heated (150 °C, 2 min) to form a $HPbI_3$ thin film. In Figure 2B (left), which is an optical image with superimposed PL map, the initial as-synthesized $HPbI_3$ film shows highly heterogeneous morphology and incomplete coverage, and as expected no PL emission is observed within the detection limit. Upon exposure to CH_3NH_2 gas at room temperature for 2 s (Figure 2B center), the $HPbI_3$ grains have disappeared showing null optical contrast and PL signal that of a nonluminescent liquid. Upon degassing for 2 s (Figure 2B right), a strongly luminescent $MAPbI_3$ film readily appears with uniform coverage on the substrate. The $MAPbI_3$ perovskite phase in that film is confirmed by XRD (Figure S2), which shows strong absorption in the UV−vis spectrum (Figure S3). The intermediate liquid phase is clearly the result of the strong interaction between $HPbI_3$ solid and CH_3NH_2 gas, and its amorphous structure and transparent nature are revealed by XRD and UV−vis in Figure S4, respectively. Through careful weighing of the initial $HPbI_3$ powder and the liquid (Figure S5A), it is determined that the liquid contains ~4.5 CH_3NH_2 per $HPbI_3$. From stoichiometry considerations, this is reminiscent of the $MAPbI_3{\cdot}xCH_3NH_2$ ($x \sim 3.5$) intermediate liquid phase that forms when $MAPbI_3$ solid uptakes CH_3NH_2 gas molecules via

DOI: 10.1021/jacs.5b11824
J. Am. Chem. Soc. 2016, 138, 750−753

"metastable" interaction in our previous report.[11] It is observed (Figure S6) that such CH_3NH_2-uptake behavior does not occur when the $MAPbI_3$ is heated to an elevated temperature (150 °C), indicating that "metastable" interaction observed at room temperature is unfavorable at 150 °C. Therefore, a set of control *in situ* optical and PL microscopy experiments were conducted at 150 °C to gain insight into the origin of the ~4.5 CH_3NH_2 uptake per $HPbI_3$ at room temperature.

Figure 2C shows the morphological evolution of a $HPbI_3$ crystal upon treatment of CH_3NH_2 at 150 °C using optical microscopy. It can be seen the $HPbI_3$ crystal darkens progressively upon exposure to CH_3NH_2, (Figure 2C), but even after 30 min exposure there is no formation of liquid or change in the morphology of the crystal. The corresponding results from the $HPbI_3$ thin film are presented in Figure 2D. Upon exposure to CH_3NH_2 gas at 150 °C for 5 s (Figure 2D, center), some PL signal is observed. After 20 s (Figure 2D, right) all the $HPbI_3$ grains in the film have transformed to $MAPbI_3$ without significant change in the film morphology; the PL map mirrors the heterogeneity and the partial coverage of the initial $HPbI_3$ thin film. The XRD pattern (Figure S7) and UV−vis absorption spectrum (Figure S3) of the resultant film confirm $MAPbI_3$ perovskite phase.[5] The striking contrast between the homogeneous, full-coverage morphology of the final $MAPbI_3$ thin films obtained by room-temperature CH_3NH_2-gas treatment (Figure 2B, right) and the heterogeneous, partial-coverage morphology obtained at 150 °C (Figure 2D, right) indicates that the $MAPbI_3$ perovskite reconstruction via the $MAPbI_3$-CH_3NH_2 "metastable" interaction does not occur in the latter. This is also supported by the distinct crystallographic characteristics (texture, etc.) of the two $MAPbI_3$ films as revealed by the XRD patterns (Figures S2 and S7). Thus, at elevated temperature, only 1 CH_3NH_2 is uptaken per $HPbI_3$, resulting in the formation of a stoichiometric $MAPbI_3$ perovskite via stable ionic/covalent interaction (rxn 1). This is further supported by careful weighing experiments (Figure S5B). Therefore, the 4.5 CH_3NH_2 uptaken by $HPbI_3$ at the CH_3NH_2-exposure stage at room temperature includes two parts: 1 CH_3NH_2 that is responsible for the stoichiometric formation of $MAPbI_3$ nuclei and 3.5 CH_3NH_2 that rapidly "melts" the as-nucleated $MAPbI_3$ perovskite. As the CH_3NH_2-uptake behavior occurs at the molecular scale, these two parts appear to occur simultaneously (Figure 2A,B), resulting in the formation of the intermediate $MAPbI_3{\cdot}3.5CH_3NH_2$ liquid phase, where the excess 3.5 CH_3NH_2 is subsequently released upon degassing due to the "metastable" nature of the original 3.5 CH_3NH_2 uptake (rxn 2).

$$HPbI_3(s) + CH_2NH_2(g) \rightarrow MAPbI_3(s) \quad (1)$$

$$HPbI_3(s) + (1 + x)CH_3NH_2(g) \rightarrow MAPbI_3{\cdot}xCH_3NH_2(l) \rightarrow MAPbI_3(s) + xCH_3NH_2(g) \quad (2)$$

The room-temperature interaction between the nanoscale film of $HPbI_3$ and the CH_3NH_2 gas occurs within seconds (rxn 2), which opens up a remarkable opportunity to form ultrasmooth $MAPbI_3$ perovskite thin films using this facile chemical route, as shown schematically in Figure 3. First, upon simple exposure to CH_3NH_2 gas, the nominally solution-deposited $HPbI_3$ film (rough, partial coverage) uptakes $(1 + x)$ CH_3NH_2, converting it into a smooth "liquid" film of $MAPbI_3{\cdot}xCH_3NH_2$ that spreads over the whole substrate. This step is the result of the "shape-preserved" perovskite formation with 1 CH_3NH_2 uptake, followed rapidly by perovskite "melting" process with excess x CH_3NH_2 uptake (indicated by dashed arrows in Figure 3). Upon

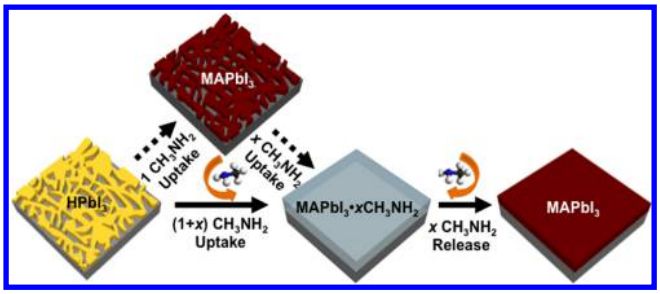

Figure 3. Schematic representation of the room-temperature formation of ultrasmooth, full-coverage $MAPbI_3$ perovskite film from the interaction of rough, partial-coverage $HPbI_3$ thin film with CH_3NH_2 gas.

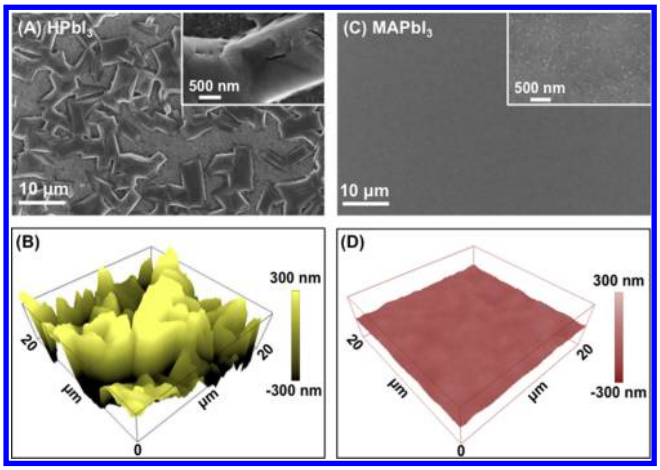

Figure 4. SEM images of: (A) the starting rough, partial-coverage $HPbI_3$ thin film and (C) the corresponding converted smooth, full-coverage $MAPbI_3$ thin film after CH_3NH_2 treatment at RT. AFM images of: (B) the starting rough, partial-coverage $HPbI_3$ thin film and (D) the corresponding converted smooth, full-coverage $MAPbI_3$ thin film after CH_3NH_2 treatment at RT.

the removal of CH_3NH_2 atmosphere, supersaturation occurs rapidly with the release of x CH_3NH_2, resulting in the crystallization of the ultrasmooth stoichiometric $MAPbI_3$ perovskite thin film.[12]

The scanning electron microscope (SEM) images in Figure 4A show the top-surface morphology of the as-deposited $HPbI_3$ film at low and high magnifications, respectively. The poor quality of the $HPbI_3$ film with only ~50% coverage is clearly evident in Figure 4A. The underlying substrate is visible in Figure 4A inset corner. The atomic force microscope (AFM) image in Figure 4B confirms the rough surface, with a high root-mean-square (RMS) roughness of ~180 nm. After CH_3NH_2-gas exposure for 2 s at room temperature followed by degassing for 2 s, the converted $MAPbI_3$ perovskite film appears remarkably uniform and full-coverage in the top-surface SEM images in Figure 4C. The AFM image in Figure 4D further demonstrates the uniform morphology and the smoothness (RMS roughness ~6 nm) of the $MAPbI_3$ perovskite film over a 20 × 20 μm^2 area. This confirms that the morphology of the resulting $MAPbI_3$ perovskite is nearly independent of the morphology of the nominally processed $HPbI_3$ solid precursor film, which is the direct result of the underlying transformative film-evolution mechanism illustrated in Figure 3.

PSCs were then fabricated using the $MAPbI_3$ perovskite thin films deposited using the method described above. Cross-sectional SEM image of a typical PSC (fractured) is shown in

DOI: 10.1021/jacs.5b11824
J. Am. Chem. Soc. 2016, 138, 750−753

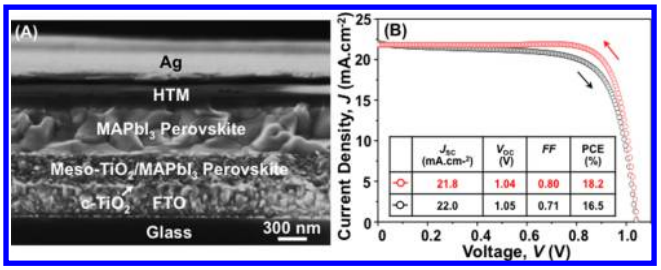

Figure 5. (A) Cross-sectional SEM of a typical PSC (fractured) fabricated using the $HPbI_3$-CH_3NH_2 precursor-pair based deposition method. (B) *J*−*V* responses under forward and reverse scans.

Figure 5A. The various layers are visible in that micrograph and are labeled as such: glass/FTO, c-TiO_2, meso-TiO_2/$MAPbI_3$ perovskite, $MAPbI_3$ perovskite (capping layer), hole-transporting material (HTM), and Ag top contact. The mesoporous TiO_2 layer is tightly infiltrated with the fully converted phase-pure perovskite (Figure S8) forming a bicontinuous structure with a dense perovskite capping layer, as shown in Figure S9. Current density−voltage (*J*−*V*) responses in Figure 5B from the champion PSC (cell area 0.12 cm^2) show a PCE of 16.4% and 18.2% in forward and reverse scans, respectively, under one sun illumination (AM 1.5G, 100 $mW{\cdot}cm^{-2}$). Since the typical *J*−*V* hysteresis is observed, stabilized PCE and *J* output at maximum power point (MPP) were measured over a period of 100 s under continuous one sun illumination and are plotted in Figure S10; a stabilized PCE of ∼17.1% and *J* of 19.5 $mA{\cdot}cm^{-2}$ are reported. The external quantum efficiency measurement (Figure S11) shows an integrated current density consistent with the J_{SC}. The PCE of small-area (0.12 cm^2) PSCs shows a tight distribution (Table S1). Figure S12 shows *J*−*V* response for a large-area PSC (1.17 cm^2) with a PCE of 14.5% (see Figure S13 for the MPP stabilized *J* and PCE output), which is close to the-state-of-the-art square-centimeter area PSCs,[13] attesting to scalability of this $MAPbI_3$ perovskite thin films deposition method based on the $HPbI_3$-CH_3NH_2 precursor pair.

In closing, we have observed a strong room-temperature solid−gas interaction behavior between the $HPbI_3$-CH_3NH_2 precursor pair, which shows promise for the deposition of high-quality $MAPbI_3$ perovskite thin films for high-PCE PSCs. This strong precursor interaction results in ultrasmooth, full coverage $MAPbI_3$ perovskite thin films, which is virtually independent of the poor morphology of the starting $HPbI_3$ precursor films, making this deposition process highly robust. The chemical origins responsible for the transformative evolution of $MAPbI_3$ perovskite thin films are elucidated. This study highlights the significance of precursor interaction chemistry in the formation of high-quality hybrid perovskite thin films, which is playing a central role in the scalable production of high-PCE PSCs of the future.

■ ASSOCIATED CONTENT

Supporting Information

The Supporting Information is available free of charge on the ACS Publications website at DOI: 10.1021/jacs.5b11824.

Experimental details and data (PDF)

■ AUTHOR INFORMATION

Corresponding Authors

*kai.zhu@nrel.gov
*nitin_padture@brown.edu
*cuigl@qibebt.ac.cn

Author Contributions

#These authors contributed equally.

Notes

The authors declare no competing financial interest.

■ ACKNOWLEDGMENTS

S.P., Z.W, Z.Z., and G.C. acknowledge the support from the International S&T Cooperation Program of China (2015DFG62670), the Youth Innovation Promotion Association of CAS (2015167), the Qingdao Key Lab of solar energy utilization and energy storage technology. Y.Z., A.R.K., and N.P.P acknowledge the support from the National Science Foundation (award nos. DMR-1305913 and OIA-1538893) for the work performed at Brown University. M.Y. and K. Z. acknowledge the support from the U.S. Department of Energy SunShot Initiative under the Next Generation Photovoltaics 3 program (DE-FOA-0000990) for the work performed at the National Renewable Energy Laboratory (contract no. DE-AC36-08-GO28308).

■ REFERENCES

(1) Kojima, A.; Teshima, K.; Shirai, Y.; Miyasaka, T. *J. Am. Chem. Soc.* **2009**, *131*, 6050.
(2) (a) Kim, H.-S.; Lee, C.-R.; Im, J.-H.; Lee, K.-B.; Moehl, T.; Marchioro, A.; Moon, S.-J.; Humphry-Baker, R.; Yum, J.-H.; Moser, J. E.; Grätzel, M.; Park, N.-G. *Sci. Rep.* **2012**, *2*, 591. (b) Stranks, S. D.; Snaith, H. J. *Nat. Nanotechnol.* **2015**, *10*, 391. (c) Grätzel, M. *Nat. Mater.* **2014**, *13*, 838. (d) Yang, W. S.; Noh, J. H.; Jeon, N. J.; Kim, Y. C.; Ryu, S.; Seo, J.; Seok, S. I. *Science* **2015**, *348*, 1234. (e) www.nrel.gov/ncpv/images/efficiency_chart.jpg; NREL: Golden, CO, accessed 1/1/2016.
(3) (a) Jeon, N. J.; Noh, J. H.; Kim, Y. C.; Yang, W. S.; Ryu, S.; Seok, S. I. *Nat. Mater.* **2014**, *13*, 897. (b) Zhou, Y.; Yang, M.; Wu, W.; Vasiliev, A. L.; Zhu, K.; Padture, N. P. *J. Mater. Chem. A* **2015**, *3*, 8178. (c) Zhao, Y.; Zhu, K. *J. Phys. Chem. Lett.* **2014**, *5*, 4175.
(4) Burschka, J.; Pellet, N.; Moon, S.-J.; Humphrey-Baker, R.; Gao, P.; Nazeeruddin, M. K.; Grätzel, M. *Nature* **2013**, *499*, 316.
(5) (a) Xiao, Z.; Bi, C.; Shao, Y.; Dong, Q.; Yuan, Y.; Wang, C.; Gao, Y.; Huang, J. *Energy Environ. Sci.* **2014**, *7*, 2619. (b) Zhou, Y.; Yang, M.; Vasiliev, A. L.; Garces, H. F.; Zhao, Y.; Wang, D.; Pang, S.; Zhu, K.; Padture, N. P. *J. Mater. Chem. A* **2015**, *3*, 9249. (c) Kutes, Y.; Ye, L.; Zhou, Y.; Pang, S.; Huey, B. D.; Padture, N. P. *J. Phys. Chem. Lett.* **2014**, *5*, 3335.
(6) (a) Chen, Q.; Zhou, H.; Hong, Z.; Luo, S.; Duan, H.-S.; Wang, H.-H.; Liu, Y.; Li, G.; Yang, Y. *J. Am. Chem. Soc.* **2014**, *136*, 622. (b) Hu, H.; Wang, D.; Zhou, Y.; Zhang, J.; Lv, S.; Pang, S.; Chen, X.; Liu, Z.; Padture, N. P.; Cui, G. *RSC Adv.* **2014**, *4*, 28964.
(7) (a) Ahn, N.; Son, D.-Y.; Jang, I.-H.; Kang, S. M.; Choi, M.; Park, N.-G. *J. Am. Chem. Soc.* **2015**, *137*, 8696. (b) Wang, Z.; Zhou, Y.; Pang, S.; Xiao, Z.; Zhang, J.; Chai, W.; Xu, H.; Liu, Z.; Padture, N. P.; Cui, G. *Chem. Mater.* **2015**, *27*, 7149.
(8) Wang, F.; Yu, H.; Xu, H.; Zhao, N. *Adv. Funct. Mater.* **2015**, *25*, 1120.
(9) Shi, D.; Adinofi, V.; Comin, R.; Yuan, M.; Alarousu, E.; Buin, A.; Chen, Y.; Hoogland, S.; Rosenberger, A.; Katsiev, K.; Losovyj, Y.; Zhang, X.; Dowben, P. A.; Mohammed, O. F.; Sargent, E. H.; Bakr, O. M. *Science* **2015**, *347*, 519.
(10) Clarke, J. B.; Hastie, J. W.; Kihlborg, L. H. E.; Metselaar, R.; Thackeray, M. M. *Pure Appl. Chem.* **1994**, *66*, 577.
(11) Zhou, Z.; Wang, Z.; Zhou, Y.; Pang, S.; Wang, D.; Xu, H.; Liu, Z.; Padture, N. P.; Cui, G. *Angew. Chem., Int. Ed.* **2015**, *54*, 9705.
(12) Zhou, Y.; Game, O. S.; Pang, S.; Padture, N. P. *J. Phys. Chem. Lett.* **2015**, *6*, 4827.
(13) (a) Yang, M.; Zhou, Y.; Zeng, Y.; Jiang, C.-S.; Padture, N. P.; Zhu, K. *Adv. Mater.* **2015**, *27*, 6363. (b) Chen, W.; Wu, Y.; Yue, Y.; Liu, J.; Zhang, W.; Yang, X.; Chen, H.; Bi, E.; Ashraful, I.; Grätzel, M.; Han, L. *Science* **2015**, *350*, 944.

DOI: 10.1021/jacs.5b11824
J. Am. Chem. Soc. 2016, 138, 750−753